Time domain analysis of scattering by a water droplet

Philip Laven

9 Russells Crescent, Horley, RH6 7DJ, United Kingdom (philip@philiplaven.com)

Received 23 May 2011; revised 21 July 2011; accepted 21 July 2011;
posted 3 August 2011 (Doc. ID 147993); published 23 August 2011

Rainbows, coronas and glories are caused by the scattering of sunlight from water droplets in the atmosphere. Although these optical phenomena are seen fairly frequently, even scientifically minded people sometimes struggle to provide explanations for their formation. This paper offers explanations of these phenomena based on numerical computations of the scattering of a 5 fs pulse of red light by a spherical droplet of water. The results reveal the intricate details of the various scattering mechanisms, some of which are essentially undetectable except in the time domain.

OCIS codes: 010.1290, 240.6690, 290.4020, 320.2250.

1. Introduction

The apparently trivial process of scattering of sunlight by spherical drops of water can produce a wide range of optical phenomena including beautifully colored rainbows, coronas and glories. Careful observations of such phenomena can provide information about the size of the water droplets, but reveal no information about the relative importance of various scattering processes, such as diffraction, reflection, transmission, surface waves, etc.

Mie theory offers a rigorous solution to the problem of scattering of light by a homogeneous spherical particle, as in Fig. 1, which shows the results of Mie calculations for scattering of red light by a water droplet of radius $r = 10\,\mu$m. The intricate ripples on the curves of intensity in Fig. 1 indicate that scattering, even in the simple case of a spherical droplet, is a complicated process. Although "diffraction" is readily identifiable as the cause of scattering in the near-forward direction (e.g., for $\theta < 5°$), it is not easy to explain the other features of Fig. 1.

Fortunately, calculations using the Debye series [1–3] can give us greater understanding of the scattering mechanisms, as shown in Fig. 2. The curves labeled $p = 0$ show scattering caused by diffraction and by reflection from the exterior of the spherical particle: this combination of different scattering processes for $p = 0$ is a computational necessity to ensure convergence of the Debye series. The $p = 1$ curves show scattering involving direct transmission through the spherical particle (i.e., with no internal reflections). The $p = 2$ curves show scattering involving one internal reflection, whereas the $p = 3$ curves involve two internal reflections, and so on.

The $p = 0$ curves in Fig. 2 confirm that near-forward scattering is due to diffraction. The $p = 1$ curves are dominant when $10° < \theta < 75°$—suggesting that the ripple structure in this zone shown in Fig. 1 is caused by interference between the $p = 0$ and $p = 1$ components. This interpretation is confirmed by the fact that the maximum/minimum ratio of the ripples in Fig. 1 is greatest when $\theta \approx 75°$, which coincides with the crossing point of the $p = 0$ and $p = 1$ curves for perpendicular polarization in Fig. 2. The maximum of the $p = 2$ curve for perpendicular polarization at $\theta \approx 142°$ corresponds to the primary rainbow, while the maximum of $p = 3$ curve at $\theta \approx 125°$ corresponds to the secondary rainbow. Both the $p = 2$ and $p = 3$ curves are dominated by perpendicular polarization. Having seen the Debye series results in Fig. 2, we can now return to Fig. 1 and, with the benefit of hindsight, recognize that $p = 2$ and $p = 3$ scattering is responsible for most of the scattering shown for $120° < \theta < 180°$.

Although the Debye series calculations can identify scattering contributions of order p, they cannot distinguish between different scattering mechanisms within a given value of p. For example, it has already been noted that the Debye $p = 0$ term includes diffraction and external reflection.

0003-6935/11/280F29-10$15.00/0

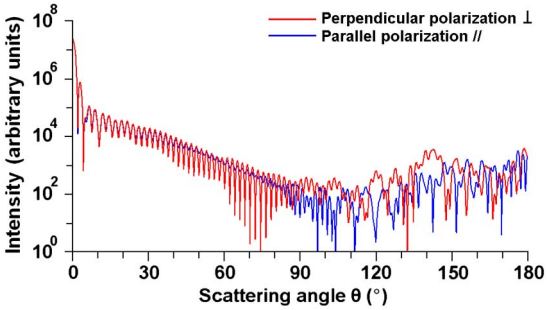

Fig. 1. (Color online) Results of Mie theory calculations for scattering of red light (650 nm) by a spherical droplet of water of radius $r = 10\,\mu$m. The refractive index of the sphere $n_1 = 1.33257 + i1.67\text{E} - 08$, while the refractive index of the medium $n_0 = 1$.

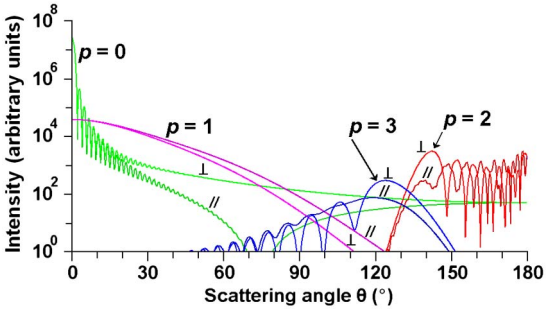

Fig. 2. (Color online) As Fig. 1, except for the use of Debye series calculations. The symbol ⊥ denotes perpendicular polarization, while the symbol // denotes parallel polarization.

This paper analyzes scattering in the time domain to understand the relative contributions made by the various scattering processes. Section 2 employs geometrical optics to provide an introduction to scattering by a spherical droplet of water in the time domain. Section 3 uses Mie and Debye series calculations to determine the impulse response at a single scattering angle $\theta = 150°$ when a water droplet is illuminated by a 5-femtosecond pulse of red light. Section 4 extends this analysis to show how the impulse response varies with scattering angle θ for Debye series $p = 0$ through $p = 3$ terms, thus identifying the contributions made by various scattering mechanisms.

2. Geometrical Optics

Geometrical optics is appealing because it offers a simple and intuitive explanation for some optical phenomena, such as rainbows. However, it fails to deal with diffraction, surface waves and, indeed, with interference phenomena. The latter failing can be partially addressed by taking account of the relative amplitudes and phases of rays that emerge from the spherical particle at a given scattering angle θ.

Geometrical optics cannot match the accuracy of Mie theory or the Debye series. The greatest limitation of geometrical optics is that it is quantitatively valid only for large particles. Nevertheless, ray tracing is a useful starting point for investigations of

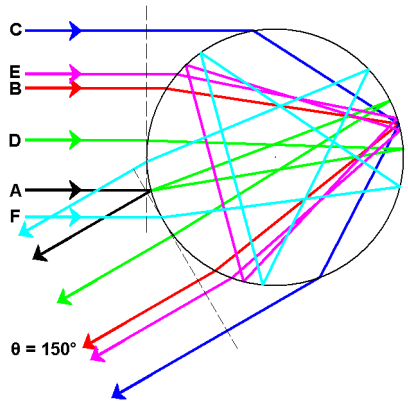

Fig. 3. (Color online) Geometric rays for $p \le 5$ that contribute to scattering at $\theta = 150°$ assuming that the refractive index of sphere $n_1 = 1.33257$ and the refractive index of medium $n_0 = 1$.

scattering mechanisms. Figure 3 shows a sphere illuminated by a beam of light, which can be considered as an infinite set of parallel rays arriving from the left of the diagram. Selected geometric rays are shown in Fig. 3 because they result in $\theta = 150°$ for $p \le 5$ (i.e., for rays suffering four or fewer internal reflections). Each of these rays is defined by p and an impact parameter b. Note that $b = 0$ indicates a "central" ray aimed at the center of the sphere, while $b = \pm 1$ indicates "edge" rays that are tangential to the top (or bottom) of the sphere. Although the individual rays in Fig. 3 all leave the sphere at $\theta = 150°$, they take very different paths—and consequently have varying path lengths. The time delay τ (measured between the dashed reference lines representing the entrance and exit planes) can be calculated using the following equation:

$$\tau = 2r/c[n_0[1 - \sqrt{(1 - b^2)}] + n_1 p \cos[\arcsin(bn_0/n_1)]], \quad (1)$$

where:

b is the impact parameter;
r is the radius of the sphere;
n_1 is the refractive index of the sphere;
n_0 is the refractive index of the medium;
c is the speed of light in a vacuum.

Rays A-F shown in Fig. 3 are just a few of the geometric rays that result in $\theta = 150°$. Many more rays for higher values of p also result in $\theta = 150°$ (some of which are listed in Table 1), but it is reasonable to assume that most of these higher order rays will produce relatively weak scattering.

3. Impulse Response at $\theta = 150°$

Table 1 suggests that, in principle, the individual ray paths shown in Fig. 3 could be identified by transmitting a short pulse of light toward the spherical particle and by measuring the time of arrival of the pulses as received by a detector located at $\theta = 150°$. In practice, it would be difficult to perform

Table 1. Propagation Parameters for Geometric Rays Resulting in $\theta = 150°$, Assuming a Sphere of Radius $r = 10\,\mu$m, Refractive Index of Sphere $n_1 = 1.33257$ and Refractive Index of Medium $n_0 = 1$

Ray	p	b	τ (fs)
A	0	−0.2588	2.3
B	2	0.5351	173.1
C	2	0.9862	175.1
D	4	0.1307	354.2
E	5	0.6475	404.1
F	5	−0.4686	423.6
G	6	0.9198	426.2
H	6	−0.7876	455.6
I	6	0.0747	532.4
J	7	0.4249	595.7
K	7	0.3056	608.5
L	8	0.6562	634.9
M	8	0.5608	656.2

such an experiment, but numerous authors have performed numerical computations using Mie theory to determine the impulse response of a spherical particle at a given value of θ. [4–13] Their results have potential applications for particle-sizing and determination of refractive index, but the specific aim of this paper is to use such techniques to obtain greater understanding of the various scattering mechanisms.

All of the results in this paper have been generated using the MiePlot computer program which can be downloaded free of charge from www.philiplaven.com/mieplot.htm. The MiePlot program first performs a fast Fourier transform (FFT) on the pulse shape in the time domain to determine the spectrum of the pulse, which is then multiplied by the results of scattering calculations for a range of scattering angles θ at a number of discrete wavelengths across the bandwidth of the pulse. The results for a given value of θ as a function of wavelength are then subjected to another FFT so as to produce the time domain impulse response for that value of θ. Figure 4 shows the calculated impulse response for scattering angle $\theta = 150°$ for the following conditions:

- Nominal wavelength: $\lambda = 650$ nm;
- Pulse duration: $t_0 = 5$ fs (half-amplitude duration with pulse shape defined by amplitude $E = 0.5[1 + \cos(\pi t/t_0)]$ for $-t_0 < t < t_0$);
- Pulse bandwidth: 564 nm–767 nm at −3 dB points; but the bandwidth of the pulse has been truncated at −40 dB points (404 nm–1664 nm);
- Sphere radius $r = 10\,\mu$m;
- Refractive index of sphere: $n_1 = 1.33257 + i1.67\text{E} - 08$ at nominal wavelength $\lambda = 650$ nm (N.B. The real part of the refractive index of water is 1.344 at 404 nm and 1.313 at 1664 nm, while the imaginary part is negligible for the current purposes.);
- Refractive index of medium: $n_0 = 1$.

Figures 4(a) and 4(b) have been calculated using Mie theory, while Fig. 4(c) has been calculated using the Debye series so as to separate scattering contributions for various values of p. Figures 4(b) and 4(c) have been calculated using a fixed value of refractive index of the sphere across the bandwidth of the pulse (i.e., $n_1 = 1.33257 + i1.67\text{E} - 08$).

The effects of dispersion can be seen by comparing Figs. 4(a) and 4(b). The $p = 0$ pulse at $\tau \approx 2$ fs is due to reflection from the exterior of the sphere, corresponding to ray A in Fig. 3. Note that the $p = 0$ pulses have essentially identical shapes in Figs. 4(a) and 4(b), thus indicating that dispersion has little or no effect

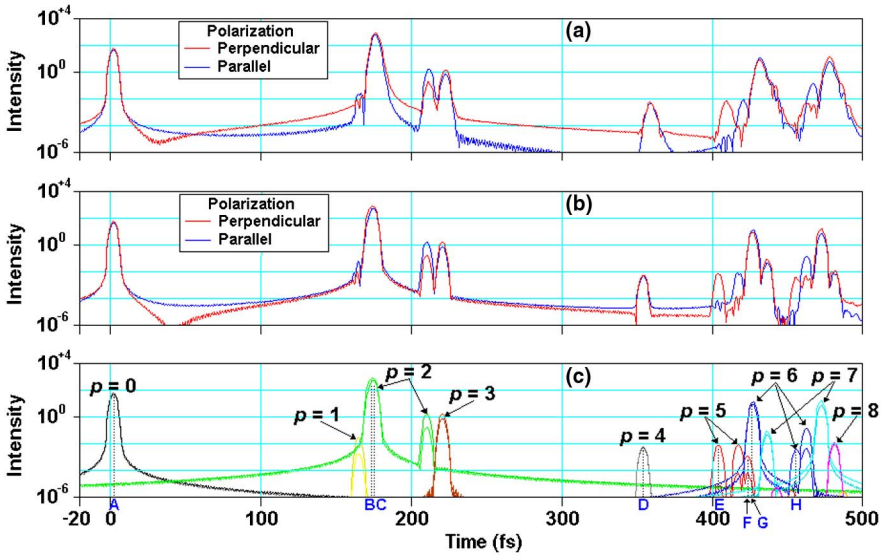

Fig. 4. (Color online) Impulse response of a water droplet of radius $r = 10\,\mu$m for a 5 fs pulse of red light (nominal wavelength $\lambda = 650$ nm) at scattering angle $\theta = 150°$. Graph (a) takes account of dispersion (i.e., due to the varying refractive index n_1 of the sphere across the bandwidth of the pulse). Graph (b) assumes that the refractive index of the sphere $n_1 = 1.33257 + i1.67\text{E} - 08$ and that this does not change with wavelength. Graph (c) uses Debye series calculations to identify scattering caused by specific values of p. The letters A to H correspond to the time delays τ specified in Table 1.

on these pulses. But, for $p > 0$, the pulses in Fig. 4(a) are broadened and slightly shifted in time relative to Fig. 4(b). For example, the $p = 4$ pulses have very different shapes and, furthermore, show maximum intensity at $\tau = 359.1$ fs in Fig. 4(a) and $\tau = 354.2$ fs in Fig. 4(b).

Although the Figs. 4(b) and 4(c) incorrectly assume that the refractive index of the sphere n_1 is independent of wavelength, several of the pulses in Fig. 4(c) coincide with the timings from Table 1, as indicated by the dotted vertical lines marked A to H. This close agreement between the values of τ given by the various independent methods of calculation (i.e., Mie, Debye and ray-tracing) gives considerable confidence in the results.

However, it is also important to acknowledge that some of the scattered pulses shown for $\theta = 150°$ in Fig. 4(c) were not predicted by the ray-tracing exercise in Fig. 3—for example, there is a $p = 1$ pulse at $\tau \approx 165.2$ fs, a $p = 2$ pulse at $\tau \approx 210$ fs, a $p = 3$ pulse at $\tau \approx 220$ fs, and a $p = 5$ pulse at $\tau \approx 416$ fs. What causes these "nongeometrical" pulses?

4. Impulse Response as a Function of θ

It is clear that examining the impulse response at a particular scattering angle θ can give valuable information about the scattering processes at that value of θ. However, even more information is revealed if the impulse response is displayed as a function of θ, as in Fig. 5, which shows the impulse responses from $\theta = 0°$ to $\theta = 180°$ in 0.2° steps. The intensity of the scattered pulses is coded according to the false-color scale shown above the diagram. The maximum intensity occurs for $p = 0$ at $\theta = 0°$ (forward scattering) and $\tau \approx 67$ fs. Note that the time reference ($\tau = 0$) corresponds to $p = 0$ reflection from the exterior of the sphere at $\theta = 180°$.

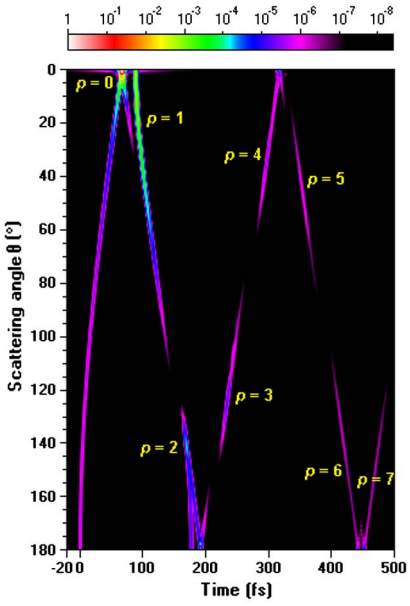

Fig. 5. (Color online) Mie theory calculations of the impulse response of a water droplet of radius $r = 10\,\mu$m for a 5 fs pulse of red light (nominal wavelength $\lambda = 650$ nm) as a function of scattering angle θ. The refractive index of the sphere $n_1 = 1.33257 + i1.67\text{E} - 08$ and the refractive index of the medium $n_0 = 1$ are assumed to be constant across the bandwidth of the pulse. The intensity of the scattered pulses is coded according to the false-color scale shown above the diagram.

Figure 5 has been calculated using Mie theory, but Debye series calculations have been used to identify the order p of the scattering processes. To facilitate comparisons with the results of ray tracing, Fig. 5 and all of the subsequent calculations reported in this paper assume that the refractive index of water $n_1 = 1.33257 + i1.67\text{E} - 08$ does not vary with wavelength.

A. $p = 0$ Scattering

Figure 6(a) shows the impulse response calculated using the Debye series for $p = 0$ (external reflection and diffraction). The impulse response in Fig. 6(a) can be considered as the sum of the impulse responses shown in Figs. 6(b) and 6(c). Figure 6(b) shows the impulse response due solely to reflection from the exterior of the sphere—as shown by the parametric curve marked with the values of the impact parameter b obtained from ray-tracing calculations. In this case, a ray with $b = 0$ results in $\theta = 180°$ and $\tau = 0$, while a ray with $b = 1$ results in $\theta = 0°$ and $\tau = 66.7$ fs. The latter value of τ corresponds to the propagation delay ($2r/c$) that would be experienced by a ray with $\theta = 0°$ in the absence of the sphere. Note that the false colors in Fig. 6(b) are identical to those in the comparable parts of Fig. 6(a)—except when $\theta < 10°$ where Fig. 6(a) is dominated by the contributions shown in Fig. 6(c). This close agreement shows that calculations using geometrical optics can give accurate results in terms of the intensity of external reflection. Similarly, the time delays predicted by geometrical optics precisely match those predicted by the Debye series calculations. The inverted v-shape centered on $\tau = 66.7$ fs in Fig. 6(c) represents diffraction. [14,15] The process of diffraction is usually thought of as a wave phenomenon, but this inverted v-shape suggests that diffraction could be considered as a two-ray interference pattern as proposed by Keller in his geometrical theory of diffraction [16,17]. For monochromatic light, interference between the two propagation paths indicated by the inverted v-shape in Fig. 6(c) results in a series of maxima and minima as a function of θ, thus producing a corona, which is a system of circular rings centered on $\theta = 0°$. Scattering of white light produces the atmospheric corona, which appears as colored rings surrounding the sun or the moon. As diffraction is essentially independent of the refractive index n_1, the angular size of the corona is determined solely by the size of the water droplets.

B. $p = 1$ Scattering

Figure 7 compares the results of Debye series and geometrical optics calculations for $p = 1$ scattering as a function of θ for $n_1 = 1.33257$. The results are identical when θ is small, but the intensity of

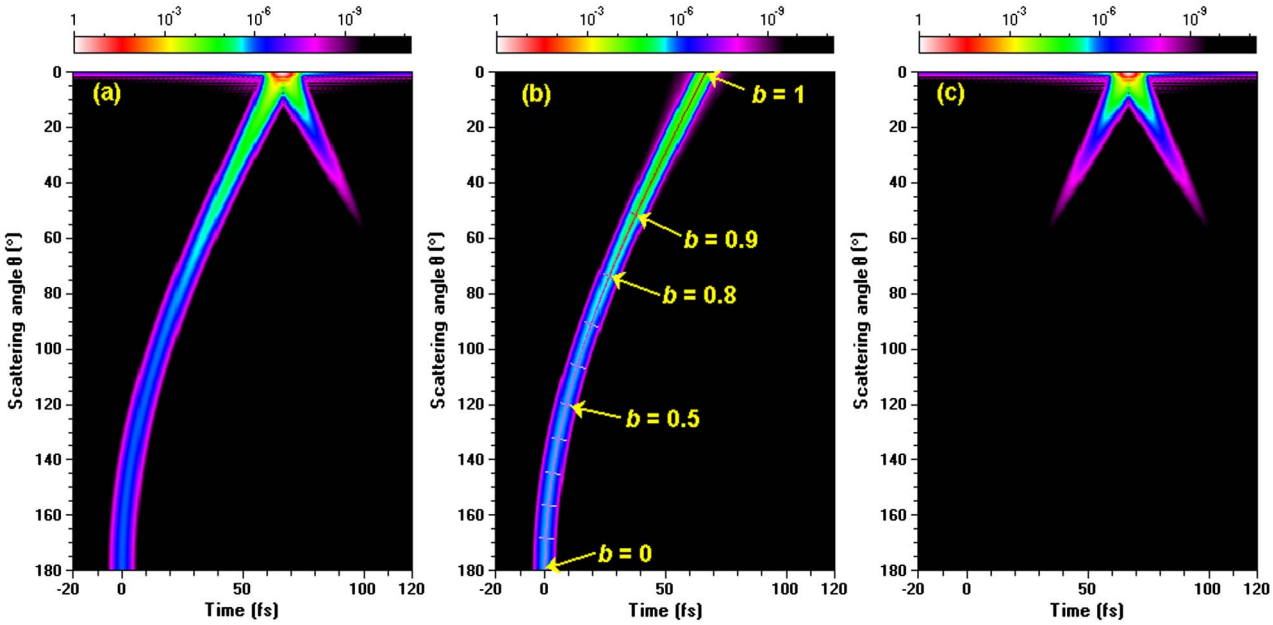

Fig. 6. (Color online) $p = 0$ impulse response as a function of scattering angle θ calculated using (a) Debye series calculations, (b) geometrical optics calculations for reflection from exterior of the droplet, and (c) the diffraction term. Note that (a) shows the result of combining (b) and (c).

geometrical optics contribution falls to zero at $\theta_c = 180° - 2\sin^{-1}[1/n_1] \approx 82.75°$. Although geometrical optics makes no contribution to $p = 1$ scattering when $\theta > \theta_c$, the Debye results include the contributions of surface waves, thus showing no discontinuity in the region around θ_c. Surface waves shed radiation continuously as they propagate around the surface of the sphere. As Fig. 7 has a logarithmic vertical axis, the fact that Debye results are almost straight lines when $100° < \theta < 150°$ implies that the attenuation of surface waves is roughly proportional to the angular distance traveled by the surface waves. In general, contributions from surface waves can generally be identified by (a) straight line portions of graphs of intensity as a function of scattering angle (when a logarithmic intensity scale is used) and by (b) the dominance of parallel polarization. The series of maxima and minima as θ approaches 180° in Fig. 7 corresponds to the $p = 1$ glory, which can be understood more easily in the time domain.

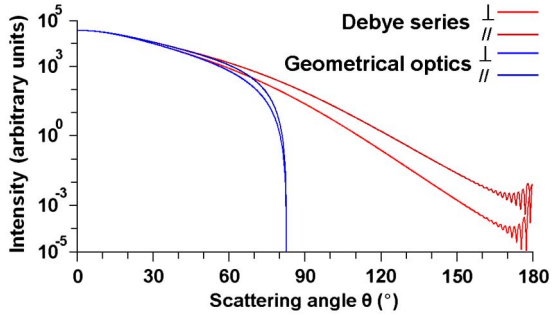

Fig. 7. (Color online) Intensity of $p = 1$ scattering as a function of scattering angle θ, calculated using Debye series and geometrical optics. The symbol $\perp$ denotes perpendicular polarization, while the symbol // denotes parallel polarization.

Figure 8(a) shows the impulse response calculated using the Debye series for $p = 1$ (transmission through the sphere with no internal reflections). Again, the time delays calculated by ray-tracing have been superimposed on the curves: in this case, a ray with $b = 0$ gives $\theta = 0°$ and $\tau = 88.8$ fs, while a ray with $b = 1$ gives $\theta = \theta_c \approx 82.75°$ and $\tau = 125.4$ fs. Figure 8(b) shows a comparable diagram calculated using geometrical optics. The lower portion of Fig. 8(b) is black, emphasizing that, as noted above, no $p = 1$ geometric rays result in $\theta > 82.75°$. The similarity of the colors for $\theta < 70°$ in Figs. 8(a) and 8(b) indicates that the intensity of scattering predicted by geometrical optics is close to that predicted by the rigorous Debye series calculations—but Fig. 8(b) also shows that the intensity of the geometrical optics contribution decreases very rapidly as θ approaches 82.75°.

Figure 8(a) shows significant $p = 1$ scattering for $\theta > 82.75°$ and $\tau > 125.4$ fs (as highlighted by the dashed lines). The colors in Fig. 8(a) show that intensity of this scattering decreases smoothly as θ is increased with the notable exception of a slight increase in intensity when $\theta > 175°$. The v-shaped pattern centered on $\tau \approx 183$ fs in Fig. 8(a) shows two $p = 1$ pulses as $\theta \to 180°$. Taking the example of $\theta = 150°$, Fig. 8(a) indicates a pulse at $\tau \approx 165$ fs with another much weaker pulse at $\tau \approx 201$ fs. We have already seen evidence of the former pulse in Fig. 4(c), which shows a $p = 1$ pulse at $\tau \approx 165.2$ fs, but the latter pulse is too weak to be seen in Fig. 4(c) because it is obscured by other pulses.

Figure 9 attempts to identify the propagation paths corresponding to these two additional $p = 1$ pulses. The top diagram in Fig. 9 shows an incident

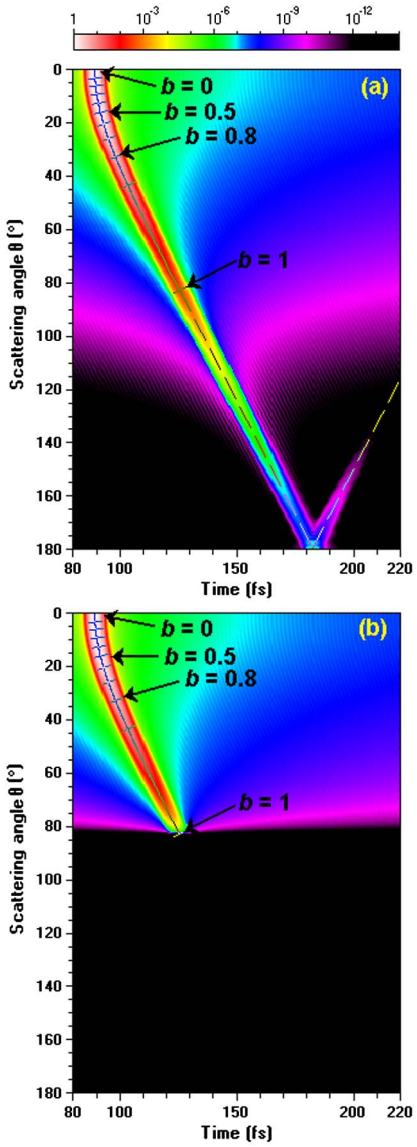

Fig. 8. (Color online) $p = 1$ impulse response as a function of scattering angle θ calculated using (a) Debye series and (b) geometric optics.

ray arriving from the left of the diagram with impact parameter $b = 1$. This ray is refracted into the sphere at point A and then travels to point B generating surface waves which travel along an arc of 67.3° from B to C on the circumference of the sphere, resulting in $\theta = 150°$. The bottom diagram shows an incident ray with impact parameter $b = -1$, which is refracted at point D and travels within the sphere to point E generating surface waves along a circular arc of 127.3° from E to F. In this case, the total counterclockwise deviation is 210°, which is equivalent to the required value of $\theta = 150°$. The two propagation paths shown in Fig. 9 can be described respectively as "short-path" and "long-path" $p = 1$ surface waves. In general, when $\theta = 180° - \delta$, the long-path surface wave travels an angular distance along the circumference of the sphere that is 2δ longer than the short-path surface wave—e.g., as shown in Fig. 9 for $\theta = 150°$,

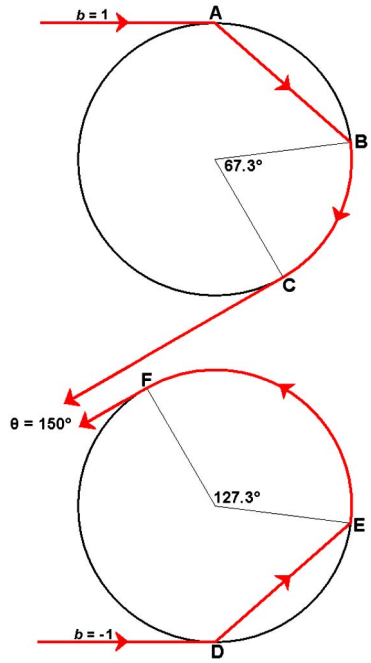

Fig. 9. (Color online) Two $p = 1$ propagation paths involving surface waves resulting in $\theta = 150°$.

corresponding to $\delta = 30°$, the difference in arc lengths is 60°.

Assuming that surface waves propagate at the speed of light c, the calculated time delays for these two propagation paths shown in Fig. 9 are $\tau = 164.5$ fs and $\tau = 199.4$ fs. Detailed analysis [18] of the propagation speed of surface waves indicates that, for the conditions applicable in this paper, surface waves can be considered to travel around the surface of the spherical particle at about $0.98c$, in line with earlier theoretical studies [19]. Taking account of this factor means that the two pulses shown in Fig. 9 should occur at $\tau = 165.3$ fs and $\tau = 200.9$ fs, which can be compared with the values of $\tau \approx 165.2$ fs and $\tau \approx 200.7$ fs obtained from the Debye series calculations in the time domain. This excellent agreement provides compelling evidence of the contributions made by surface waves to $p = 1$ scattering [3,20].

Armed with this insight into the propagation of surface waves, we can see that the $p = 1$ glory is the result of interference between scattered light that has followed two counter-rotating propagation paths. As already noted, the v-shaped pattern centered on $\tau \approx 183$ fs in Fig. 8(a) indicates that two $p = 1$ pulses can be observed as $\theta \to 180°$. The two pulses can easily be distinguished in the time domain by using a pulse duration of 5 fs, as shown in Fig. 8(a), except when the two scattered pulses are separated by less than about 10 fs (i.e., when $\theta > 175°$).

For continuous-wave illumination (as in Fig. 7), constructive interference occurs when the difference Δ in path length between the two propagation modes is $\Delta = m\lambda$, where m is an integer. For $\theta = 180° - \delta$, the path length differs by $\Delta = 2\pi r(2\delta/360°)$ where δ is measured in degrees. When $r = 10\,\mu$m and

$\lambda\times = 650 \times \times$ nm, maxima should occur when δ is a multiple of 1.86° (i.e., at $\theta = 180°$, 178.1°, 176.4° and 174.1°) corresponding to the rings of the $p = 1$ glory, confirming the results shown for parallel polarization in Fig. 7. As δ increases, the "long-path" surface wave contribution becomes much weaker than the "short-path" surface wave contribution, thus explaining why the glory appears only when δ is small —i.e., when $\theta \to 180°$. Although the Debye calculations for $p = 1$ scattering show clear evidence of a glory when $\theta \to 180°$, this glory is much weaker than the scattering for other values of p—and, hence, it cannot be observed in practice. Nevertheless, the $p = 1$ glory is worth studying because, as will be seen in the next section, the atmospheric glory caused by $p = 2$ scattering is formed by similar processes.

C. $p = 2$ Scattering

Figure 10 shows the intensity of $p = 2$ scattering (caused by one internal reflection in the sphere) calculated using the Debye series. The maximum intensity occurring at $\theta \approx 142°$ and $\tau \approx 170$ fs corresponds to the primary rainbow. Although this diagram is more complicated than Figs. 6 and 8, much of it can be explained by reference to the results of ray-tracing calculations, which have been superimposed on Fig. 10 as parametric curves as a function of b. In this case, $b = 0$ corresponds to a ray that passes through the center of the sphere and then suffers an internal reflection and is scattered at $\theta = 180°$ (backscattering) with delay $\tau = 177.7$ fs. As b increases, the value of θ reduces until it reaches its minimum value at the geometric primary rainbow angle $\theta_{r1} = 137.9°$ when $b = 0.8611$. Further increases in b cause θ to increase until $\theta = 165.5°$ when $b = 1$. Note that geometrical optics predicts maximum intensity at $\theta_{r1} = 137.9°$, whereas the Debye calculations show a maximum at $\theta \approx 142°$. Despite this difference, it is interesting to realize that geometrical optics shows that the minimum value of time delay τ occurs at θ_{r1}—implying that the rainbow corresponds to the shortest path (as well as the maximum intensity).

Two geometric rays cause scattering when $137.9° < \theta < 165.5°$. Interference between these two rays causes the supernumerary arcs on the primary rainbow—which appear in Fig. 2 as maxima and minima of the $p = 2$ curve. Figure 10 shows that the results of the Debye $p = 2$ calculations agree very well with the time delays from ray-tracing calculations for $0 \le b \le 1$.

These calculations have been made for spherical droplets of water with radius $r = 10\,\mu$m, which are typical of fog rather than rain. With such small droplets, the rainbow (known as a fogbow) tends to be almost white, instead of the brilliantly colored rainbows that are produced by raindrops of larger radius, such as $r = 500\,\mu$m or more. Calculations in the time domain of $p = 2$ scattering caused by large drops of water produce diagrams very similar to Fig. 10, except that the time delays are much larger due to size of the drops.

As with $p = 1$ scattering, surface waves play a significant role in $p = 2$ scattering, as indicated by the dashed lines starting from $\theta = 165.5°$ and $\tau = 184.1$ fs. Looking at the results for $\theta = 150°$, we can see a $p = 2$ pulse at $\tau \approx 210$ fs, which also appears in Fig. 4. Figure 11 offers an explanation for this nongeometrical pulse: an incident ray with $b = -1$ suffers one internal reflection before generating surface waves, which propagate along an arc of 44.5° before leaving the sphere at $\theta = 150°$. Assuming that surface waves travel at $0.98c$ around the circumference of the sphere, this propagation path would correspond to $\tau = 210.5$ fs.

As surface waves are the dominant cause of the atmospheric glory, it is worth looking in more detail at Fig. 10, specifically as θ approaches 180°, where the two dashed lines converge at $\theta = 180°$ and $\tau = 192.7$ fs to produce a v-shaped pattern. When the difference in the time delays is less than the duration of the incident pulse (5 fs), the two pulses (one due to "short-path" $p = 2$ surface waves and the other due to "long-path" $p = 2$ surface waves) merge into a single pulse. The intensity of the resulting pulse depends on the relative phase of the two components,

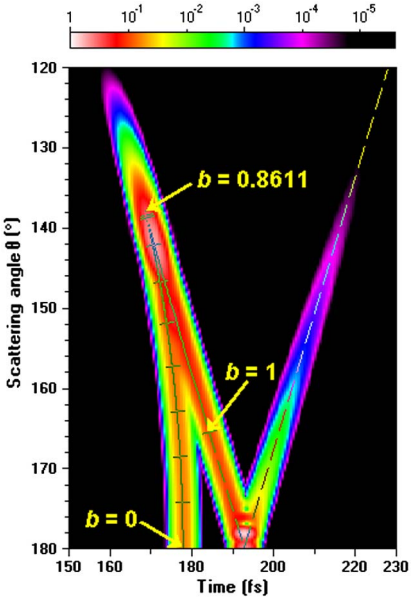

Fig. 10. (Color online) $p = 2$ impulse response as a function of scattering angle θ calculated using the Debye series.

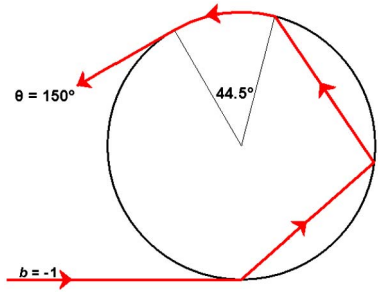

Fig. 11. (Color online) $p = 2$ propagation path involving surface waves resulting in $\theta = 150°$.

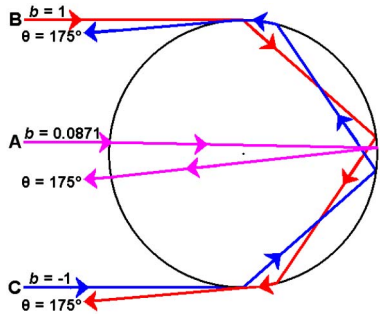

Fig. 12. (Color online) Three $p = 2$ propagation paths resulting in $\theta = 175°$. Ray A is a geometrical ray, whereas rays B and C involve surface waves.

just as it does for illumination by a continuous-wave source of light. Figure 10 shows increased intensity at $\theta \approx 178°$ due to constructive interference between the two components.

Figure 12 shows that there are three $p = 2$ propagation paths that result in scattering at $\theta = 175°$. Ray A with $b = 0.0871$ is a geometric ray that suffers one internal reflection giving $\theta = 175°$ with $\tau = 177.5$ fs. Ray B with $b = 1$ suffers one internal reflection and generates surface waves that travel approximately 9.5° along the surface of the spherical particle, giving $\theta = 175°$ with $\tau = 189.7$ fs. Similarly, Ray C with $b = -1$ suffers one internal reflection and generates surface waves that travel approximately 19.5° along the surface of the spherical particle, resulting in $\theta = 175°$ with $\tau = 195.7$ fs. Note that Rays B and C travel in opposite directions around the water droplet: the resulting interference pattern between the short-path and long-path surface waves corresponds to the glory [20].

Although Fig. 12 is concerned only with scattering at $\theta = 175°$, Fig. 13 shows the intensity of the scattering contributions for $170° < \theta < 180°$ due to type A, B and C propagation paths (i.e., the contributions due to near-central $p = 2$ reflections, the "short-path" and "long-path" $p = 2$ surface waves, respectively). Figure 13 has been derived from time domain calculations for a 5 fs pulse, which does not achieve complete separation of the scattered pulses of type B and C for $\theta > 175°$, but good separation is possible for $\theta < 174°$. Figure 13 shows that propagation paths involving surface waves (type B and C) are dominated by parallel polarization—and, perhaps, surprisingly that short-path surface waves (type B) give stronger scattering than the near-central geometrical reflection (type A).

In summary, $p = 2$ scattering is responsible for the primary rainbow with the supernumerary arcs being caused by interference between two geometric rays that both result in scattering at a specific value of θ despite having followed different paths through the water drop. Note that the geometric primary rainbow angle θ_{r1} is dependent on the refractive index n_1 of water. As n_1 varies with wavelength λ, θ_{r1} also varies with λ—for example, when $\lambda = 400$ nm, $n_1 = 1.3445$, and $\theta_{r1} = 139.6°$ and when $\lambda = 700$ nm, $n_1 = 1.3314$, and $\theta_{r1} = 137.7°$. This indicates that the primary rainbow has a width of about 2° between the red and violet arcs. On the other hand, $p = 2$ propagation paths trigger counter-rotating surface waves that result in the colored rings of the atmospheric glory centered on $\theta = 180°$ (the anti-solar point)—in this case, the angular size of the glory is determined by the size of the water droplet rather than being determined by the refractive index n_1 [21].

D. $p = 3$ Scattering

Figure 14 shows the intensity of $p = 3$ scattering (caused by two internal reflections in the sphere)

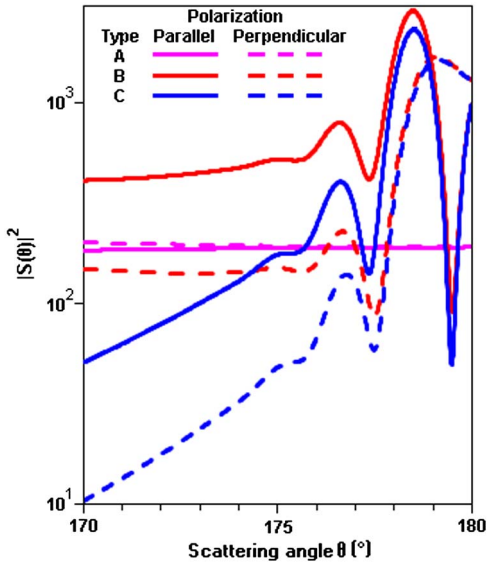

Fig. 13. (Color online) Intensity of $p = 2$ scattering for propagation paths of type A, B and C as defined in Fig. 12 derived from the time domain results summarized in Fig. 10.

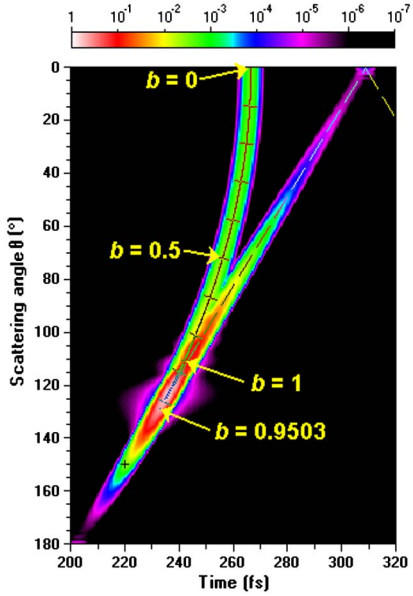

Fig. 14. (Color online) $p = 3$ impulse response as a function of scattering angle θ calculated using the Debye series.

calculated using the Debye series. The zone of maximum intensity occurring at $\theta \approx 125°$ and $\tau \approx 235\,\mathrm{fs}$ corresponds to the secondary rainbow. Many of the features of Fig. 14 can be explained by reference to ray-tracing calculations: In this case, $b = 0$ corresponds to a ray that passes through the center of the sphere and then suffers two internal reflections and is scattered at $\theta = 0°$ (forward scattering) with a delay $\tau = 266.5\,\mathrm{fs}$. As b increases, the value of θ increases until it reaches its maximum value at the geometric secondary rainbow angle $\theta_{r2} = 129.2°$ when $b = 0.9503$. Further increases in b cause θ to decrease until $\theta = 111.8°$ when $b = 1$. The effects of $p = 3$ surface waves are indicated by the dashed lines starting from $\theta = 111.8°$ and $\tau = 242.8\,\mathrm{fs}$.

Returning to Fig. 4, an unexplained $p = 3$ pulse was noted at $\tau \approx 220\,\mathrm{fs}$. This is marked in Fig. 14 by the + symbol, which coincides with the diagonal "finger" of intensity associated with the secondary rainbow at $\theta \approx 125°$ and $\tau \approx 235\,\mathrm{fs}$. As rainbows correspond to the transition between two rays and zero rays, geometrical optics predicts an abrupt transition to zero intensity in the "unlit" area at θ_{r2}. This unrealistic transition is softened by the Debye series calculations (and by Airy theory), which show decreasing intensity in the zone with no geometric rays. The $p = 3$ pulse at $\theta = 150°$ and $\tau \approx 220\,\mathrm{fs}$ is the result of a "complex ray" [3], which occurs in the zero-ray region as defined by geometrical optics. Complex rays appear on all rainbows—as can be seen by examination of Fig. 10.

5. Conclusions

Analysis of scattering in the time domain reveals a wealth of information about scattering processes that is simply not available when the scattering particle is illuminated by a continuous-wave light source. The time domain results reported in this paper for spherical droplets are based on calculations using Mie theory, the Debye series and ray tracing—with excellent agreement among all three methods. Geometrical optics is frequently considered to be inadequate for scattering from small particles, but this paper's results for scattering of red light by a water droplet of radius $r = 10\,\mu\mathrm{m}$ (corresponding to size parameter $x = 2\pi r/\lambda \approx 96$) are surprisingly accurate.

While ray tracing is obviously an approximation, it can be used to identify the propagation paths taken by geometrical rays, as well as to confirm the scattering contributions due to surface waves—such as the $p = 2$ surface waves that cause the atmospheric glory. Similarly, the ray-tracing results show that the supernumerary arcs of rainbows are due to interference between pairs of geometric rays that emerge from the scattering particle at a given scattering angle θ.

On the other hand, the time domain results for $p = 0$ show that the diffraction process (which causes the corona) is marked by a characteristic inverted v-shape pattern when the impulse response is displayed as a function of θ, suggesting that the diffraction can be considered as a two-ray interference pattern.

More generally, the time domain results reveal the intricate details of the various scattering mechanisms, some of which are essentially undetectable except in the time domain. These results can be used to provide greater understanding of light scattering by spherical particles, such as droplets of water.

The author would like to thank the two anonymous reviewers for their helpful and constructive suggestions.

References

1. P. Debye, "Das elektromagnetische Feld um einen Zylinder und die Theorie des Regenbogens," Phys. Z. **9**, 775–778 (1908).
2. B. Van der Pol and H. Bremmer, "The diffraction of electromagnetic waves from an electrical point source round a finitely conducting sphere, with applications to radiotelegraphy and the theory of the rainbow," Philos. Mag. **24**, 825–864 (1937).
3. E. A. Hovenac and J. A. Lock, "Assessing the contributions of surface waves and complex rays to far-field Mie scattering by use of the Debye series," J. Opt. Soc. Am. A **9**, 781–795 (1992).
4. E. E. M. Khaled, D. Q. Chowdhury, S. C. Hill, and P. W. Barber, "Internal and scattered time-dependent intensity of a dielectric sphere illuminated with a pulsed Gaussian beam," J. Opt. Soc. Am. A **11**, 2065–2071 (1994).
5. K. S. Schifrin and I. G. Zolotov, "Quasi-stationary scattering of electromagnetic pulses by spherical particles," Appl. Opt. **33**, 7798–7804 (1994).
6. L. Méès, G. Gouesbet, and G. Gréhan, "Scattering of laser pulses (plane wave and focused Gaussian beam) by spheres," Appl. Opt. **40**, 2546–2550 (2001).
7. L. Méès, G. Gréhan, and G. Gouesbet, "Time-resolved scattering diagrams for a sphere illuminated by plane wave and focused short pulses," Opt. Commun. **194**, 59–65 (2001).
8. Y. P. Han, L. Méès, K. F. Ren, G. Gréhan, Z. S. Wu, and G. Gouesbet, "Far scattered field from a spheroid under a femtosecond pulsed illumination in a generalized Lorenz-Mie theory framework," Opt. Commun. **231**, 71–77 (2004).
9. H. Bech and A. Leder, "Particle sizing by ultrashort laser pulses—numerical simulation," Optik **115**, 205–217 (2004).
10. H. Bech and A. Leder, "Particle sizing by time-resolved Mie calculations—A numerical study," Optik **117**, 40–47 (2006).
11. C. Calba, C. Rozé, T. Girasole, and L. Méès, "Monte Carlo simulation of the interaction between an ultra-short pulse and a strongly scattering medium: The case of large particles," Opt. Commun. **265**, 373–382 (2006).
12. S. Bakić, C. Heinisch, N. Damaschke, T. Tschudi, and C. Tropea, "Time integrated detection of femtosecond laser pulses scattered by small droplets," Appl. Opt. **47**, 523–530 (2008).
13. S. Bakić, F. Xu, N. Damaschke, and C. Tropea, "Feasibility of extending rainbow refractometry to small particles using femtosecond laser pulses," Part. Part. Syst. Charact. **26**, 34–40 (2009).
14. P. Laven, "Separating diffraction from scattering: the million dollar challenge," J. Nanophoton. **4**, 041593 (2010).
15. J. A. Lock and P. Laven, "Mie scattering in the time domain. Part 2. The role of diffraction," J. Opt. Soc. Am. A **28**, 1096–1106 (2011).
16. J. B. Keller, "A geometrical theory of diffraction," in *Calculus of Variations and Its Applications*, L. M. Graves, ed., Proceedings

of Symposia in Applied Mathematics (McGraw-Hill, 1958), Vol. 3, pp. 27–52.
17. J. B. Keller, "Geometrical theory of diffraction," J. Opt. Soc. Am. **52**, 116–130 (1962).
18. J. A. Lock and P. Laven, "Mie scattering in the time domain. Part I. The role of surface waves," J. Opt. Soc. Am. A **28**, 1086–1095 (2011).
19. H. M. Nussenzveig, "High-frequency scattering by a transparent sphere. I. Direct reflection and transmission," J. Math. Phys. **10**, 82–124 (1969).
20. P. Laven, "How are glories formed?" Appl. Opt. **44**, 5675–5683 (2005).
21. P. Laven, "Effects of refractive index on glories," Appl. Opt. **47**, H133–H142 (2008).